

M.T. Lemmon¹, R.D. Lorenz², J. Rabinovitch³, C.E. Newman⁴, N.R. Williams⁵, R. Sullivan⁶, M.P. Golombek⁵, J.F. Bell III⁷, J.N. Maki⁵, A. Vicente-Retortillo⁸

¹Space Science Institute, Boulder, CO 80301, USA. ²Applied Physics Laboratory, Laurel, MD 20723, USA. ³Stevens Institute of Technology, Hoboken, NJ, 07030, USA. ⁴Aeolis Research, Chandler, AZ, USA. ⁵Jet Propulsion Laboratory, California Institute of Technology, Pasadena, CA, USA. ⁶Cornell University, Ithaca, NY, USA. ⁷Arizona State University, Tempe, AZ, USA. ⁸Centro de Astrobiología (INTA-CSIC), Madrid, Spain.

Corresponding author: Mark Lemmon (MLemmon@SpaceScience.org)

Key Points:

- Six flights of the Ingenuity helicopter were documented with video acquired by Mastcam-Z on the Perseverance rover in Jezero crater, Mars.
- Dust mobilization was expected while the helicopter was below 1- m altitude but was observed at low wind speeds from >5 m altitude.
- Recirculating dust clouds unexpectedly formed while the helicopter was at >5 m cruising altitude.

Abstract

Martian atmospheric dust is a major driver of weather, with feedbacks between atmospheric dust distribution, circulation changes from radiative heating and cooling driven by this dust, and winds that mobilize surface dust and distribute it in the atmosphere. Wind-driven mobilization of surface dust is a poorly understood process due to significant uncertainty about minimum wind stress, and whether saltation of sand particles is required. This study utilizes video of six Ingenuity helicopter flights to measure dust lifting during helicopter ascents, traverses, and descents. Dust mobilization persisted on take-off until the helicopter exceeded 3 m altitude, with dust advecting at 4-6 m/s. During landing, dust mobilization initiated at 2.3-3.6 m altitude. Extensive dust mobilization occurred during traverses at 5.1-5.7 m altitude. Dust mobilization threshold friction velocity of rotor-induced winds during landing are modelled at 0.4-0.6 m/s (factor of two uncertainty in this estimate), with higher winds required when the helicopter was over undisturbed terrain. Modeling dust mobilization from >5 m cruising altitude indicates mobilization by 0.3 m/s winds, suggesting non-saltation mechanisms like mobilization and destruction of dust aggregates. No dependence on background winds was seen for the initiation of dust lifting, but one case of takeoff in 7 m/s winds created a track of darkened terrain downwind of the helicopter, which may have been a saltation cluster. When the helicopter was cruising at 5-6 m altitude, recirculation was seen in the dust clouds.

Plain language summary

Mars is a dusty planet with a dusty atmosphere, and dust is a major factor in the weather. Weather events, from large storms to small dust devils, raise dust in their winds, but the conditions needed to lift the dust remain elusive. We used video of six flights of the *Ingenuity* helicopter, taken by Mastcam-Z on the *Perseverance* rover, to document when and where dust lifting happened. We found that the helicopter sometimes kicked up dust when it was cruising >5 m above the surface, and that it always did when it was 1.4-3.6 m above the surface as it landed. Some of the dust was likely lifted when the winds moved sand particles, and the sand dislodged the sticky dust, as in some current models. However, some dust lifting happened with lower winds, and likely happened when large aggregates of dust (sometimes called “dust bunnies”) were dislodged and broke up.

1 Introduction

Understanding dust mobilization on Mars is essential for understanding and predicting the background atmospheric dust distribution, the onset and evolution of dust storms (the largest of which can cover the entire planet in a veil of dust for weeks on end, e.g., Guzewich et al., 2019), and the effects of lifted dust on Martian atmospheric dynamics. Due to Mars’s low atmospheric density, which absorbs and scatters relatively little solar or thermal radiation, the presence of dust in the atmosphere has a major impact on its radiative balance, which in turn strongly affects thermal gradients and winds (Wolff et al., 2017; Kahre et al., 2017). The global distribution of atmospheric dust depends on atmospheric transport, interactions with ice particles (microphysics), fallout rate, and dust mobilization from the surface. The last process is least understood and in greatest need of investigation (Newman et al., 2022a). Dust lifting has been observed in both straight-line winds and vortices (dust-devils), which may be roughly equally important both outside of dust storms (Newman et al., 2022b) and during the onset of regional storms (Lemmon et al., 2022).

Dust may be mobilized as a direct result of wind stress or indirectly because of other wind-mobilized particles, and other forces may contribute to lifting. Wind tunnel experiments utilizing flat beds of uniform particles have shown that wind mobilizes fine/very-fine sand grains more easily than either finer or coarser particles (e.g., Iversen and White, 1982), discouraging the idea that individual dust-sized particles might be directly entrained by wind. Instead, saltation, a bouncing sand grain motion, has been proposed as a prerequisite to dust mobilization, in which easier-to-move saltating sand-sized grains would disturb dust-sized particles, entraining them into the turbulent boundary layer (e.g., Greeley, 2002). However, in situ hand lens-quality images show that surface dust on Mars occurs in resolvable, sand-sized, but low-density aggregates with very weak, filamentary structures (Herkenhoff et al., 2004; Sullivan et al., 2008), which should be easier for wind to mobilize than solid sand grains of equivalent diameter (Merrison et al., 2007). Besides wind stress, Neakrase et al. (2016) identify factors contributing to dust mobilization and entrainment including pressure back-venting in the low-pressure core of vortices (Bila et al., 2020),

electrical forces (Kruss et al., 2021)., and a thermal-creep lifting that occurs in atmospheres with long mean-free paths driven by radiative heating of sediment (Kraemer et al., 2019). In addition, sand motion may be initialized by turbulent wind gusts and then be maintained by lower winds once motion has begun (Sullivan and Kok, 2017; Swann et al., 2020); this effect is larger on Mars than on Earth (Kok, 2010). Gravity-dependent cohesive forces within the sand bed could also reduce saltation thresholds on Mars relative to Earth (Musioli et al., 2018). Low pressures reduce the threshold for saltation by a factor of up to 2.5 (Swann et al., 2020).

The mechanisms that contribute to dust mobilization have not been directly observed on Mars, nor have the threshold wind conditions been directly measured. A direct measurement of friction velocity (related to wind stress by density) was made with Pathfinder’s multi-height windsocks, but this experiment did not coincide with observed lifting or grain motion (Sullivan et al., 2000). Using *Perseverance* data, dust lifting was observed only for winds (measured at 1.5 m height) >15 m/s (Newman et al., 2022b), while grain motion was associated with wind speeds (at 1.2 m height) >14.7 m/s in *InSight* data (Baker et al., 2021). Charalambous et al., (2021) used measured ~ 1.2 -m height winds and estimates of surface roughness to infer a friction velocity of 2.0 m/s while sand was in motion, but not a threshold. Estimates of threshold wind stress for saltation from sand mobility correspond to 0.7 m/s for the atmospheric densities considered in this work (Ayoub et al., 2014).

Beyond the importance of dust lifting in general on Mars, the specific problem of dust mobilization by rotor downwash is of interest in aviation—in terrestrial helicopter operations, the effect is termed ‘brownout’ (analogous to ‘whiteout’ in snow). In addition to possible degradation of optical sensor performance, lofted dust might cause triboelectric charging (e.g., Lorenz, 2020; Farrel et al., 2021). With helicopters now being considered for sample return operations at Mars, and the development of the Dragonfly rotorcraft for Titan underway, the possibility of extraterrestrial brownout means in-situ measurements at Mars have considerable value in testing the generality of brownout models (e.g., Rabinovitch et al. 2021) under physical conditions quite different from Earth.

This paper describes the *Perseverance* rover’s video documentation of six *Ingenuity* helicopter flights on Mars over April-September 2021. Each of the flights resulted in dust lifting from the Martian surface at takeoff and landing, and some flights resulted in dust lifting while at 3-5 m cruising altitude. We report on the altitudes for which dust lifting was observed, discuss inferred wind speeds and implications for dust lifting processes on Mars, and describe the dynamics of the resulting dust clouds.

2 Data and Methods

2.1 Flights

Ingenuity is a 0.49-m tall, 1.8 kg rotorcraft that was carried to the surface of Mars by the *Perseverance* rover (Balaram et al., 2021; Lorenz, 2022). It

has two counter-rotating, 1.21-m diameter rotor blades, four 0.384-m legs, a 0.136 m x 0.195 m x 0.163 m fuselage, and a solar panel (Fig. 1). It carries a monochrome camera for navigation purposes and a color “return to Earth” camera for documentation of the Martian terrain. *Ingenuity* was designed as a technology demonstration but was eventually used for reconnaissance in support of the *Perseverance* mission. It was deployed on 3 April 2021, which was Martian day (sol) 44 of the rover mission. Flights were conducted autonomously, using telemetry and navigation camera images to control flight according to pre-sequenced commands. The operation of *Ingenuity* during its first flights is described in detail in Grip et al. (2022).

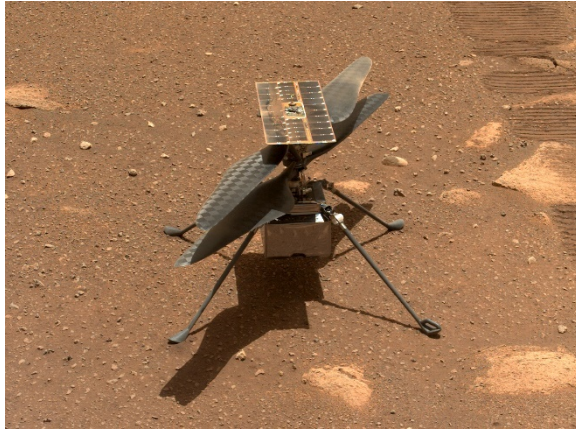


Figure 1. *Ingenuity* on Mars. This sol 47 Mastcam-Z image includes the first 3 landing sites.

The first five flights of the *Ingenuity* helicopter on Mars occurred on sols 58, 61, 64, 69, and 76. These flights were the subject of video documentation using Mastcam-Z, for the purpose of obtaining data on flight performance for engineering purposes and documenting the first flights on Mars. After flight 5, video was not acquired of most succeeding flights due to a combination of competing priorities and obstructed view; however, flight 13 was also subject to video for the purpose of documenting dust lifting.

An overview of the flight details is in Table 1. Flight 1 had a rotation and hover at 3 m above ground level (AGL). Flight 2 had a 2-m out-and-back traverse to the west (away from the rover) at 5 m AGL. Flight 3 had a 50-m out-and-back traverse to the north (out of the video frames) at 5 m AGL. Each of the first three flights took off and landed within a ~ 1 m region (Fig. 2). Flight 4 was used for reconnaissance of a new landing field, had a 133-m out-and-back traverse 10° east of south at 5 m AGL, and landed several meters from the previous landing spots. Flight 5 was a 130-m traverse 7° east of south at 5 m AGL, followed by an ascent to 10 m AGL and a landing 110 m from the rover. By flight 13, the rover and helicopter had each moved roughly 900 m to the south-southeast. Flight 13 was used for reconnaissance to the northeast, with a flight at 8 m AGL

and a landing site ~9.5 m further from the rover than the take-off site.

Table 1. Overview of flights with video.

Flight Time, UTC (2021) Sol	April 07:34	April 09:33	April 11:32	April 14:50	May 19:27	Sept. 00:08
Local	:33:13	:33:20	:33:21	:33:22	:33:17	:03:57
Mean Solar Time Duration, s						
Altitude, m					(10)	
Traverse, m						
Distance [†] , m			(63)	(75)		(310)
Zoom [‡] , mm	, 34	, 34	, 26	, 26	, 26	, 110
Rate ^{‡*} , fps	, 6.6	, 6.6	, 6.6	, 6.8	, 6.8	, 6.0
P#, Pa						**
T#, K						**
#, g m ⁻³						**
W#, m/s						**
Direction [#] °		°	°	°	°	° **

[†] Distance from rover to landing site (distance to take-off if observed and different)

[‡] Shown for left, right cameras, respectively

* Video frames per second

Average of MEDA pressure, temperature, density, and wind data at rover site over 10 minutes centered on flight

** Estimated from nearby sols

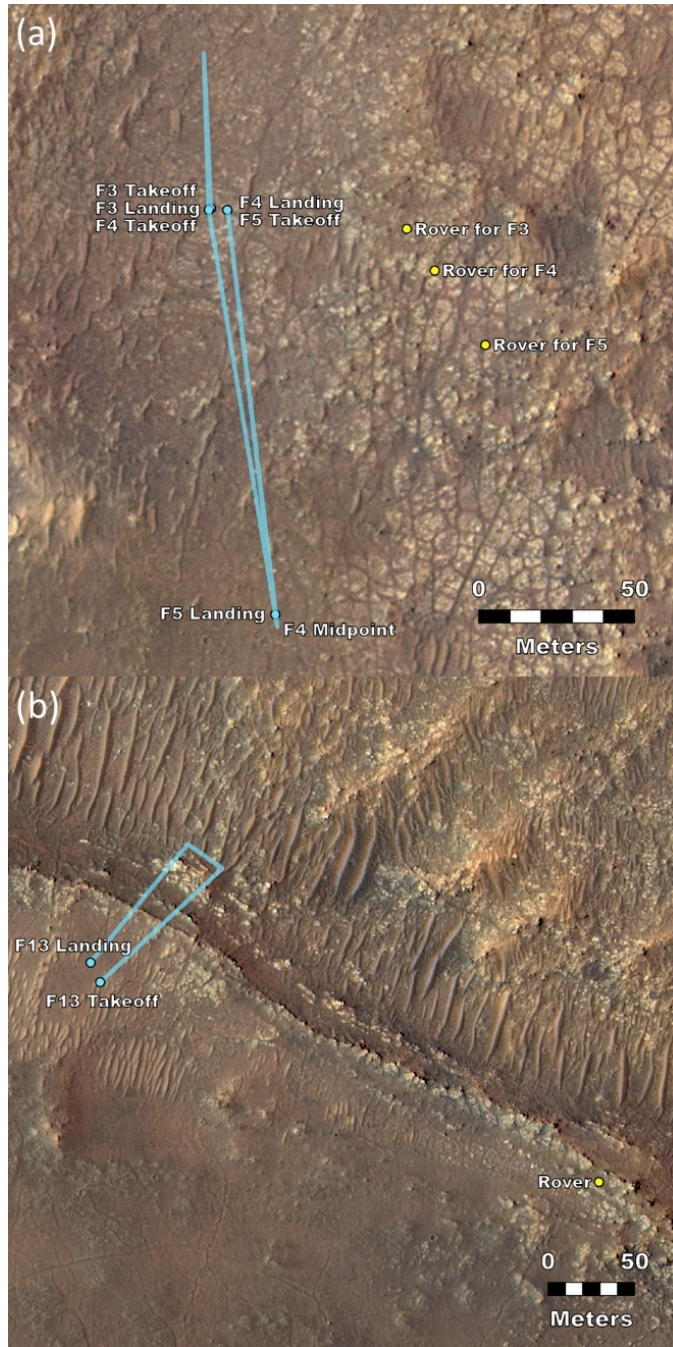


Figure 2. Flight geometry. Locations for flights 3-5 (a) and 13 (b) are shown for the rover and take-off landing sites. For flights 1-2, the rover was at the F3 location, and the takeoff and landing were indistinguishable from the F3 takeoff

position shown.

2.2 Video

Mastcam-Z is a multispectral, stereo camera system for documenting the geological and atmospheric conditions around the rover (Bell et al., 2021). Each of the left and right cameras has a zoom lens and could be independently set to 26 to 110 mm focal length. The resulting resolution is 0.423, 0.212, 0.150, and 0.673 mrad/pixel for the zoom positions of 26, 34, 48, and 110 mm, respectively, that were used for flight video (Hayes et al. 2021). The videos described here were acquired using infrared-blocking filters that resulted in red, green, and blue images when sampled through the Bayer-pattern microfilters on the Charge Coupled Device (CCD) detector (Bell et al., 2021).

The flight videos were designed for engineering support and were sequenced to maximize the frame rate within the overall system capabilities. Most videos were taken with 1280x720 pixel subframes of the 1600x1200 pixel array. They were acquired using real-time group-of-picture compression (Joint Photographic Experts Group, JPEG), such that each data product was a group of 16 consecutive frames compressed to JPEG quality 50. Most videos were much longer than the flights as a precaution against timing errors. Some video frames were deleted on board without downlink after frames that were of interest were transmitted to Earth. All videos were acquired with both eyes: in some cases, different zoom positions were used to acquire both close-up images of take-off or landing and wide-field images to maximize flight coverage; in some cases, the same zooms were used with offset subframes to increase the flight coverage (Fig. 3). For flight 5 on sol 76, the left eye was set to 110-mm zoom with a 1600x120 subframe for high-resolution and -speed documentation of the landing at a new and distant site. Each pair of videos was acquired with a fixed aim; the remote-sensing mast (RSM) was not used to re-point the cameras because tracking the helicopter was not possible.

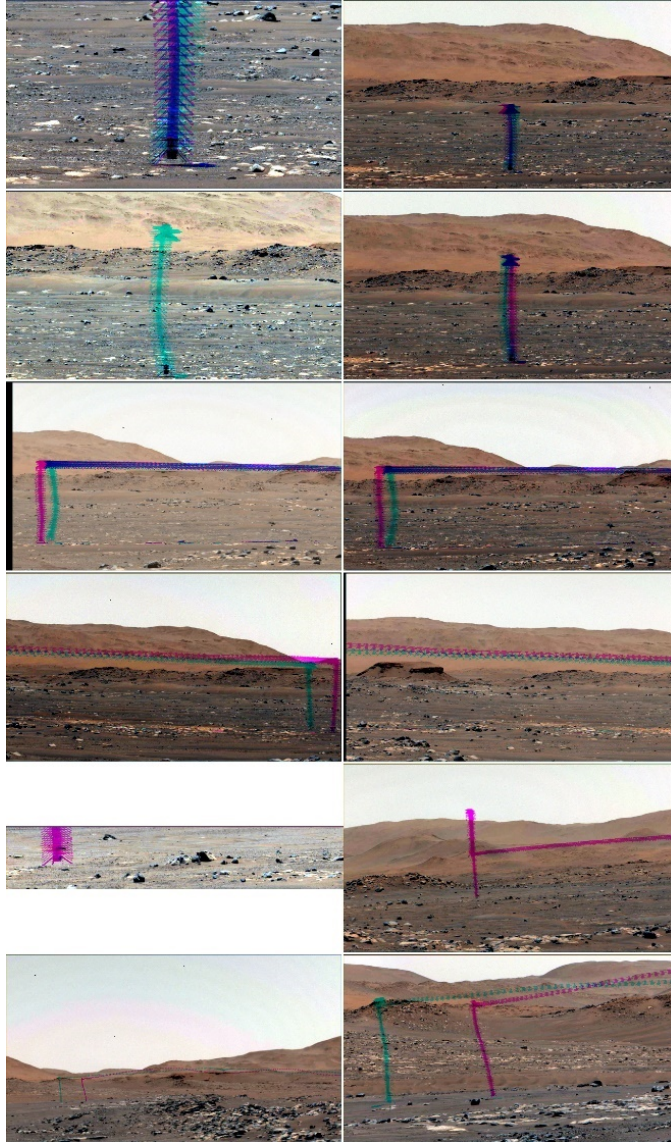


Figure 3. Video summary. Composite images are shown with a 1-99% color-stretched mean-frame image merged with helicopter positions from all frames. Mastcam-Z left eye (left) and right eye (right) images are shown for flights on sols (from top) 58, 61, 64, 69, 76, and 193. The ascent and the first half of flight are shown in teal, while last half of flight and the descent are shown in magenta; purple results from the superposition.

2.3 Additional imagery and meteorology

Ingenuity carries two cameras, described by Balaram et al. (2018). One, the

Return to Earth Camera (RTE), is a high-resolution (4208x3120 pixels), Bayer-color camera. RTE is a commercial off the shelf (COTS) Sony IMX 214, with a 47° FOV aimed ~22° below the horizon and was used for occasional images to document the terrain around the helicopter. The nadir-pointed navigation camera (NAV) is a COTS Omnivision OV7251 with 640x480 monochrome pixels and a 133°x100° FOV.

The Mars Environmental Dynamics Analyzer (MEDA) is a meteorological suite for measuring pressure, temperature, winds, humidity, and radiative fluxes (Rodriguez-Manfredi et al., 2021). It recorded data from each sensor at 1-Hz during and around each flight except for sol 193. Table 1 shows 10-minute averages for pressure, temperature, and winds; wind azimuth follows the meteorological convention of being the back-azimuth, the angle east of north from which the wind comes. Wind speed was computed via vector averaging; it was significantly different from scalar averaging of speed only for the slow winds of sol 69. On sol 193, MEDA was in safe mode and not used; estimates in Table 1 were derived from sols 190 and 194.

Low-frequency (84 Hz, 168Hz) sounds of helicopter flights 4, 5 and 6 were detected by a microphone on the SuperCAM instrument (Maurice et al., 2022). No signatures of transport generated at the distance of the helicopter were detected.

3 Results

3.1 Dust detection

Dust was visible by inspection in raw video images from some flights. To quantify dust lifting and behavior, images were processed to determine the dust amount and to produce enhanced images for the study of dust motion. The process was similar to dust devil detection and tracking algorithms (Greeley et al., 2006): it required creation of a mean frame, removal of that mean frame from individual frames, and determination of optical depth from the mean and difference frames (Fig. 4). A final step produced colorized images that enhanced the visibility of lifted dust.

For each video, mean frames were initially created from all available video frames; after initial identification of dust lifting, new mean frames were created from dust-free frames. Such frames were created for times while the helicopter was out of frame when possible and were always created for pre-take-off and post landing. For each frame, the most appropriate mean frame was used for comparison and differencing.

Optical depth was determined via a low-opacity approximation of the radiative transfer equation,

$$I = I_0 e^{-\tau} + J_0 (1 - e^{-\tau}). \text{ Eqn. 1}$$

In Eqn. 1, I is the observed radiance for each pixel and time-step, I_0 is the mean-frame radiance for each pixel, J_0 is the source function convolved with

dust scattering properties, and τ is the optical depth for each pixel and time-step. In principle, J_0 can be determined by analysis of high-contrast areas of the image with assumptions of locally uniform opacity. In practice, J_0 is nearly equivalent to the nearby sky radiance (Moores et al., 2015), which was used here. Optical depths were derived for only the green channel due to the impact of chroma noise (in the JPEG quality 50 images) on the red and blue channels. Optical depths were typically of order hundredths but averaged ~ 0.1 for the sol-64 dust cloud. Colorization was also done via an adaptation of the radiative transfer equation. The mean frame was converted to an enhanced frame by (a) multiplicatively increasing J_0 , and (b) replacing J_0 with a cyan light source, where (a) and (b) were done for each of the color channels.

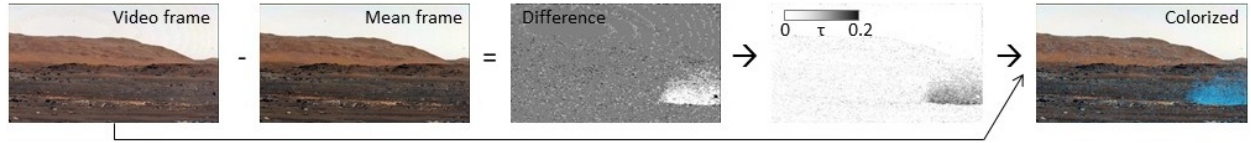


Figure 4. Illustration of opacity derivation. Each video frame was compared to an associated mean frame, resulting in a set of difference images that were converted to optical depth maps. Colorized images enhance visibility of dust with blue light.

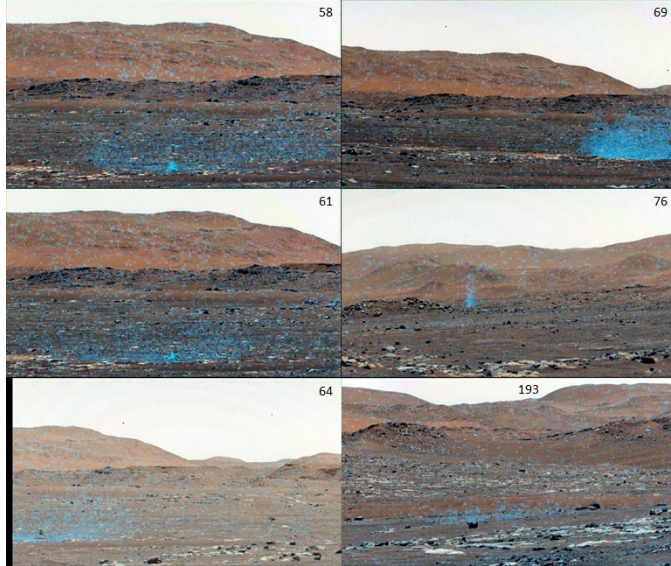


Figure 5: Dust clouds at and near landing, with colorization. Sol number of flight is indicated for each image.

All movies that showed sufficient area around the lander and included sky were processed to determine opacity. Figure 5 shows examples of the resulting enhanced images near each observed landing. Note that the sol-76 example in-

cludes a dust devil in the background. Estimated dust mass was retrieved from each image by (a) determining the area over which there was an observable dust cloud and no extraneous variability (noise or dust devil); (b) summing optical depth over all pixels in the area; and (c) converting the summed optical depth into dust mass. Because optical depth is a dimensionless optical cross-section per unit geometric cross-section, it includes particle density and the cross-sectional area and extinction efficiency averaged over the particle size distribution (PSD). For the purposes of the present calculation, a PSD representative of atmospheric dust (mean radius of $1.4\text{ }\mu\text{m}$ and mean variance of $1/3$) was used, for which it was determined that the particle volume was $0.8 \times 10^{-6}\text{ m}^3/\text{m}^2$ per unit opacity. For an assumed slightly porous density of 2000 kg/m^3 , we obtained 1.6 g/m^2 per unit opacity. The summed opacity, pixel FOV, and distance were used to determine total suspended mass over time (Fig. 6). The absolute value of the suspended mass is subject to a factor-of-a-few uncertainty due to the assumptions; relative changes are more accurate as long as the dust stays in the frame and at the same distance. In practice, the dust does neither, and the suspended dust measurement always declined after initial lifting due to a combination of motion out of the frame and increasing distance (since projected pixel area scales with D^2).

Take-off is effected by bringing the rotors with the blades set at low incidence angles (low thrust) up to operating speed (2537 rpm) and then increasing the collective pitch to near-instantaneously increase the thrust. The thrust:weight ratio initially exceeds one to leave the ground, then the helicopter ascends at $\sim 1\text{ m/s}$. For example, data from flight 1 (Lorenz, 2022, fig. 6.9) shows the collective angle, and thus thrust, had a brief ($<1\text{ s}$) pulse about 30% higher than hover values in order to break cleanly away from the surface, and then a couple of seconds at a thrust $\sim 20\%$ higher than hover in order to perform the commanded ascent (see also Grip et al., 2022). Generally, lifted dust was seen on the last frame with the helicopter on the surface, and dust lifting continued for $\sim 3\text{ s}$. All flights but 2 and 13 showed significant dust lifting while at the hover/traverse altitude. Descent involved a rapid downward acceleration followed by a constant velocity (thrust:weight ~ 1) descent to touchdown.

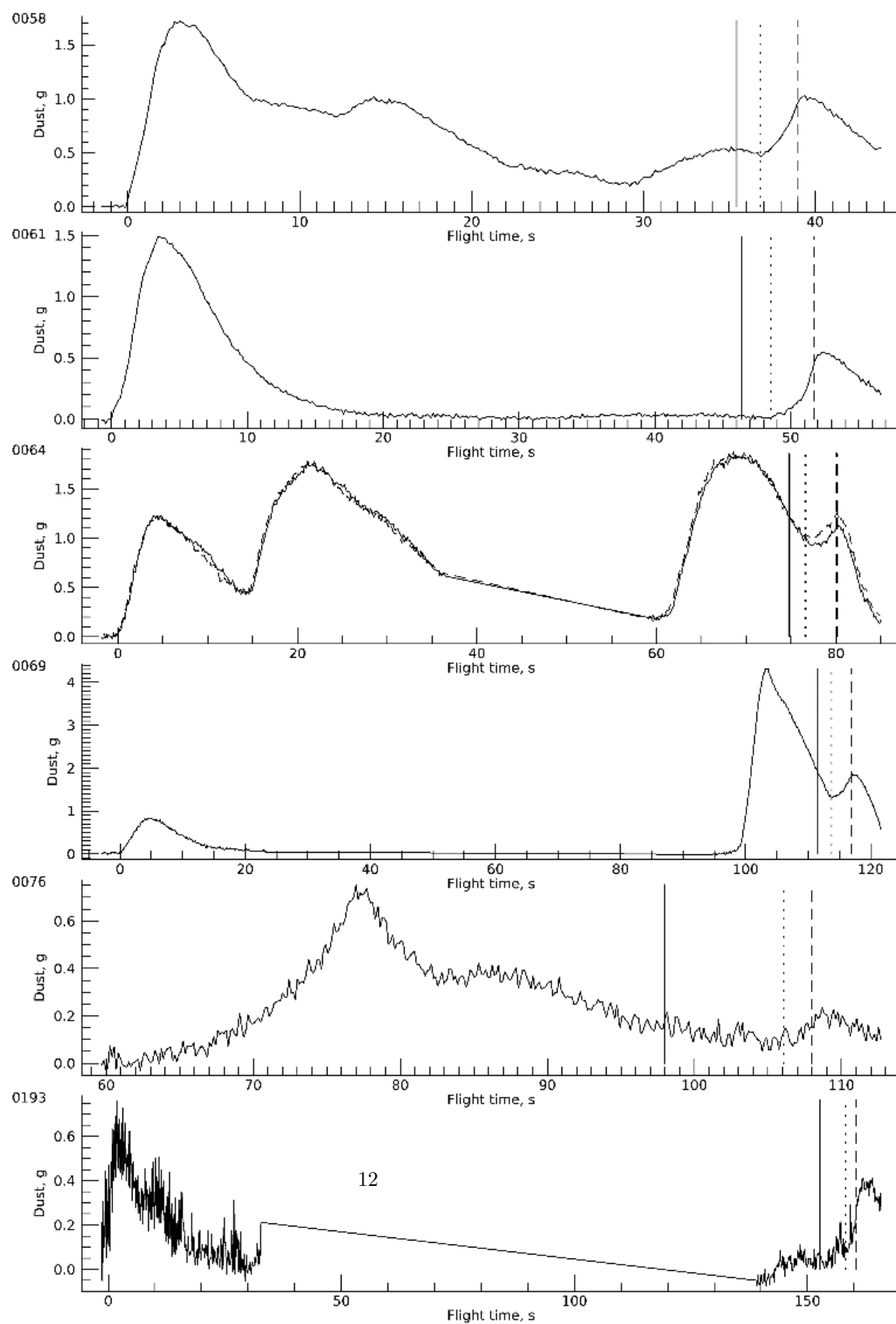


Figure 6: Suspended dust mass over time. Vertical lines mark the start of constant-speed descent (solid), visually detected dust lifting under the helicopter (dotted), and touchdown (dashed). The curves for sols 58, 61, 76, and 193 were obtained with the right eye; sol 69 with the left eye; and sol 64 with each eye (right eye dashed). From sol 64, there were times with the helicopter out of field of view that were not measured.

3.2 Flight narrative

3.2.1 Sol 58

Flight 1 caused the most observed dust lifting on takeoff, ~ 1.7 g. About 12 s into the flight, the helicopter turned in place and adjusted the thrust vector to respond to the wind and maintain station. This caused dust lifting adjacent to the area immediately below the vehicle. At 29 s, the helicopter responded to a wind causing a new burst of off-center dust lifting. Initial winds from the east-southeast carried the takeoff dust cloud to the right (rover-measured winds were from ENE). At landing, easterly winds carried dust away and to the right. Notably, the pre- and post-flight mean-frame images differed in that a darkened streak appeared along the trajectory of the take-off dust cloud: dust removal continued downwind of the helicopter and formed a dust-cleaned track (see Supplemental Information).

3.2.2 Sol 61

Flight 2 had a large burst of dust lifting on take-off and less dust lifting on landing at the same location. There was no observed dust lifting during hover or the ~ 2 m out-and-back traverse. Based on dust cloud motion, winds were away (E) and to the left (S), consistent with rover winds from ENE. No track was observed. Incidentally, a vortex was detected at the rover 63 m away, 5 minutes before take-off.

3.2.3 Sol 64

Flight 3 had comparable dust lifting on takeoff and landing as seen by both eyes. The small difference in the observed landing profiles (Fig. 6) was due to the dust moving out of frame sooner for the left eye; otherwise, the profiles are encouragingly similar. The novel aspects of flight 3 were the first traverse out of frame, and the first dust lifting along a traverse. A dust removal track was observed under the flight path. Winds measured at the rover were from the east, while the observed motion was east and north on take-off and east and south on landing. A vortex passed the rover while moving toward the helicopter ~ 20 s post-flight, with an observed 1 Pa pressure drop, 7-13 m/s counterclockwise winds, and no obvious sign of dust (*cf.* Newman et al., 2022b).

3.2.4 Sol 69

Flight 4 had no observed dust cloud along the outbound traverse. Two rover-Navcam images taken while the helicopter was out of the Mastcam-Z field of view also showed no dust lifting. When the helicopter reappeared in frame,

it was within a recirculating dust cloud that moved with the helicopter at ~ 3 m/s (to the right within the frame). During landing, the helicopter continued to circulate dust from this cloud. After landing, the dust cloud departed at ~ 1 m/s to the north, although the take-off dust cloud went west, and a distant dust devil moved north; rover-measured winds were slow and varied, mostly from the northeast. A dust removal track was observed under the flight path.

Note that while the average wind over 10 minutes around Flight #4 was quite low, there were strong turbulent gusts reaching ~ 10 m/s at the beginning of the flight. These gusts caused appreciable low-frequency acoustic noise (see Extended Data fig.1b of Maurice et al., 2022).

3.2.5 Sol 76

Take-off was not observed. After the helicopter came in frame, dust was lifted along the traverse. The cloud largely dissipated when the helicopter ascended to 10 m, and a smaller dust cloud was raised on landing. Rover-measured winds were from the ESE; several distant dust devils moved to the right (NW to W); the dust clouds lifted by the helicopter departed away and left (to S).

3.2.6 Sol 193

Dust clouds were raised only on take-off and landing. The dust clouds moved away and slightly to the right, consistent with easterly winds at the rover.

4 Discussion

4.1 Dust lifting during landing

To assess the winds associated with the observed dust lifting, we relied on the helicopter brownout model of Rabinovitch et al. (2021) which was developed early in the Ingenuity development cycle to estimate the expected severity of sediment mobilization during takeoff and landing. While a computational fluid dynamics model would allow a fuller investigation, that was out of scope of this effort. Figure 7 shows the predicted friction velocity immediately under the helicopter (at one rotor radius), adapted from Rabinovitch et al. (2021) to include the actual flight conditions (RPM, density) for thrust:weight ~ 1 conditions. We did not model take-off due to expected large departures from equilibrium, high thrust:weight, and the difficulty in determining when dust lifting ceased. However, the model was designed for the constant-speed descent; also, the initiation of dust lifting was easier to distinguish. The model predictions were compared to experiments with an analog helicopter on Earth (see Supplementary Information) and showed the predictions to be accurate to within a factor of 2, with the model overpredicting wind speed.

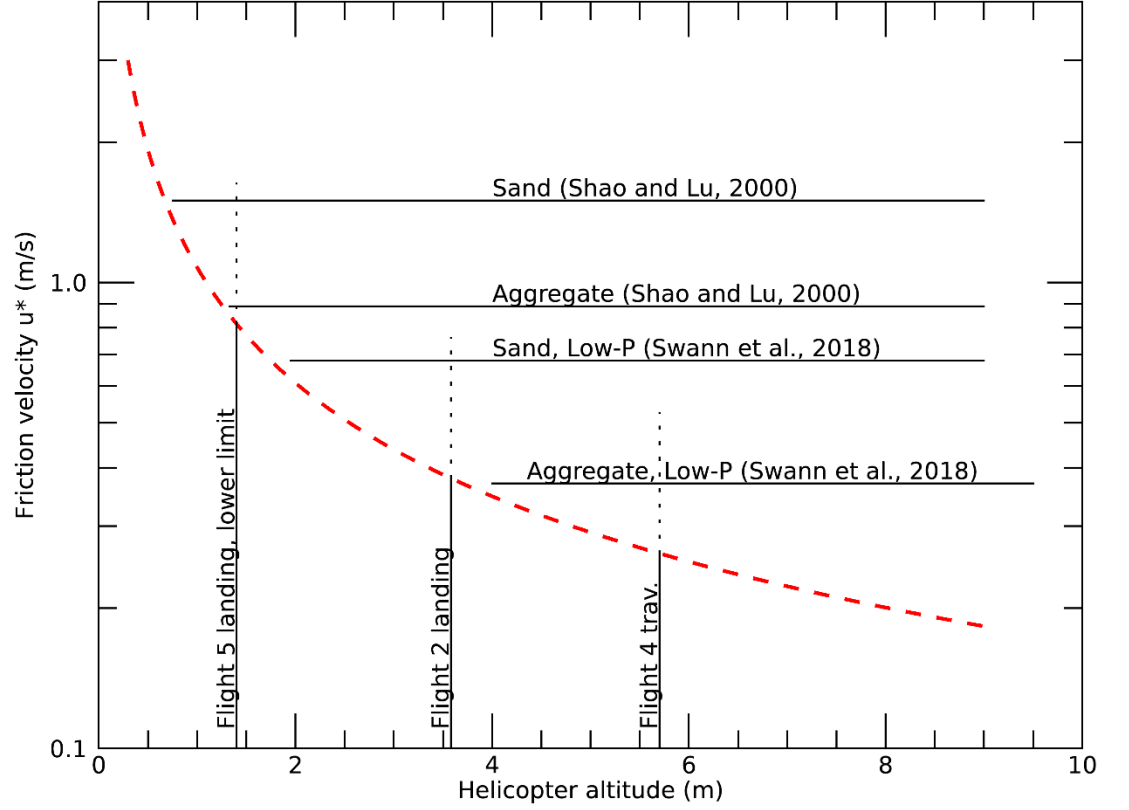


Figure 7: Friction velocity and helicopter altitude. The Rabinovitch et al. (2021) model, adapted for atmospheric density of 0.020 kg/m^3 , 2800 RPM, and Thrust:Weight=1, is shown as a red dashed line. Horizontal lines show representative thresholds for a conventional model (Shao and Lu, 2000) and a low-pressure model (Swann et al. 2018); the calculated thresholds are for mobilization of sand ($200 \text{ }\mu\text{m}$ diameter, 3200 kg/m^3) and aggregates ($500 \text{ }\mu\text{m}$, 380 kg/m^3). Vertical solid lines show representative altitudes at which dust lifting was seen during landing and traverse; dotted lines are extended upward to 2x the model prediction.

To determine a friction velocity at which dust lifting initiated, we initially inspected the images that first showed lifted dust and measured the altitude from the midpoint of the rotors to the surface at touchdown (in flight this was $\sim 30 \text{ cm}$ larger than the commanded cruise altitude). To more precisely measure the

altitude at which dust lifting initiated, and uncertainty therein, we modeled the lifted dust over time. For this, we modeled dust lifting as being 0 when the predicted u^* was below the threshold, and otherwise proportional to $(u^* - u_t^*) u^{*2}$, where u^* was the altitude-dependent prediction, u_t^* was the desired threshold friction velocity (e.g., Kawamura, 1951). The model also allowed for loss over time, parametrized as a single decay rate but representing dust that drifted out of the frame, that drifted away, and that sedimented to the surface. The results included a fit u_t^* that was dependent on the Rabinovitch et al. (2021) predictions; a robust altitude determination (that is, one that would have resulted from any reasonable model of friction velocity vs. altitude); and a dust loss rate for which we expect that geometric effects dominate the sedimentation term.

Figure 8 shows the dust within the landing area as the helicopter descended for all 6 flights, selected based on pixels that contained the dust cloud at some point near landing. Clusters of points at high altitude represent times immediately before the descent, while those at low altitude show the changing dust at near-constant altitude (the helicopter tended to bounce slightly as it contacted the surface at 1 m/s). The threshold velocity was fit for each case; for illustration purposes, Fig. 8 shows fits for $u_{*t} = 0.8, 0.55$, and 0.39 m/s. Table 2 shows each individual solution along with the corresponding altitude.

The modeled winds and observed altitudes require some dust lifting by mobilization and destruction of aggregates. Dust lifting on landing always occurred at altitudes comparable to or higher than the highest altitude for which sand saltation would be expected, as shown by the comparison of model winds and the low-pressure sand saltation model of Swann et al. (2018) in Fig. 7. The first four landings show dust lifting at friction velocities below the threshold for sand mobilization, but near or above that for low-density aggregate analogs (Merrison et al. 2007).

Analysis of dust within an even smaller region immediately around the landing site produced similar results for all but flight 4 (see Supplementary Information). For flight 4, the initiation of dust lifting under the helicopter was not visually distinguishable from the recirculating cloud, and the fit seemed influenced by spatial variations within the cloud that existed before descent. Thus, while the inflection in total dust amount over time was consistent with data from sols 61 and 64, that fit was judged less reliable.

A notable feature of the dust lifting shown in Fig. 8 is that it did not turn sharply up as the helicopter approached touchdown. In the Rabinovitch et al. (2021) model, u_* scales with $\sim h^{-0.8}$, and the drag force on particles scales as u_*^2 (Greeley and Iverson, 1985).

4.2 Dust lifting during take-off

Table 2 also reports the size of the dust clouds 2 s after liftoff and at touchdown and a measurement of dust motion. In the first frame with visible lifted dust, the diameter of the dust outline along the surface was measured. The size was measured in succeeding time steps. The rate of expansion of the dust lifting front

in Table 2 corresponds to the rate for the first two time steps; the expansion of the dust cloud slowed from frame to frame. The initial expansion was 4-6 m/s within the bottom ~5 cm of the atmosphere. We note that dust lifting in winds of those speeds is consistent with the landing measurements for surface roughness values of order 1 mm; however, they are only consistent with the absence of dust lifting for 1.5-m winds <15 m/s (Newman et al., 2022b) for surface roughness of 1 cm or greater. However, unseen small-scale vorticity likely enhanced the dust lifting.

Track formation from removal of bright dust results in a surface darkening (Charalambous et al. 2021). This was seen under the helicopters path for two traverses. Within recirculating dust clouds traveling with the helicopter, dust lifting rates were difficult to measure during the traverses. Dust removal may have been as high as 0.01-0.1 g/m², and the resulting contrast (in a heavily foreshortened view) was 2-3% darker for flight 3 and 3-4% darker for flight 4, similar to typical 2.5% drops for dust devil tracks (Reiss et al., 2016). Since a monolayer of 3- μ m dust would have a mass that is orders of magnitude less, either the dust removal was lower (e.g., spread over a larger area) or the contrast was low due to substantial remaining dust. Notably, one track, on flight 1, did not correlate with the helicopter’s position and instead moved downwind from the ascent/descent site. This may have been a saltation cluster, indicating that saltation occurred at least during take-off when u^* may have been ~2 m/s and then continued downwind, within lower wind speeds.

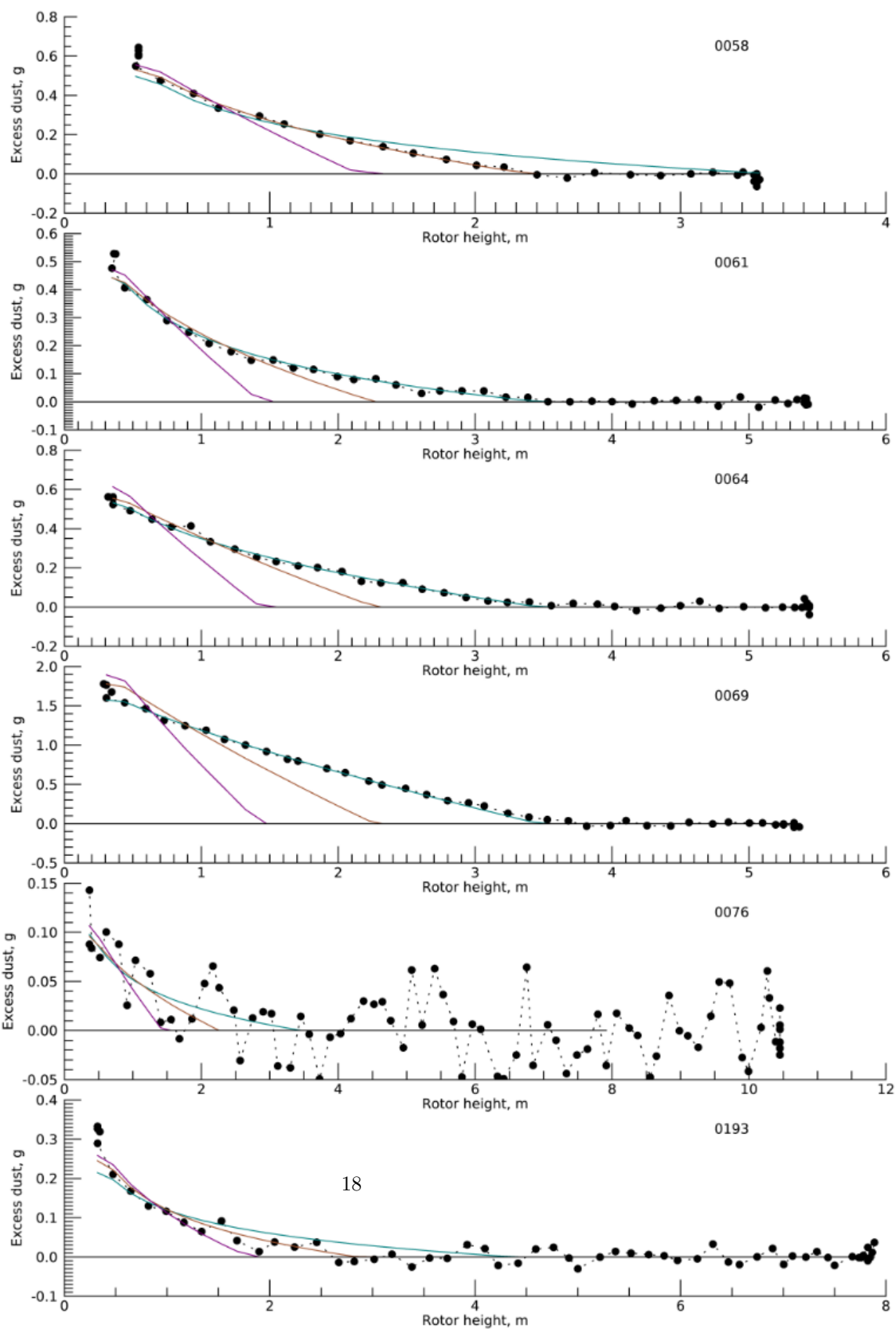


Figure 8: Lifted dust mass vs. altitude for landing dust cloud after removing background dust. Colored curves are best-fit models for $u_{*t}=0.8$ (purple), 0.55 (brown), and 0.39 (teal) m/s.

Table 2. Dust mobilization observations.

Flight						
Takeoff						
Plume radius, m, t/o+2s				>7.4	n/a	>4.6
Plume height, t/o+2s					n/a	
M_{dust} , g, t/o+2s			(L), 0.74 (R)		n/a	
U, m/s					n/a	
Landing						
Plume radius, m					n/a	
Plume height, m					n/a	
M_{dust} , g						
Z_{lift} , m [†]	±0.24	±0.24	, 0.59 ±0.22 (L) 3.06±0.32 (R)	±0.1	>1.4	-0.7/+1.2
u_{*t} , m/s [†]	±0.03	±0.02	±0.02 (L) 0.43±0.04 (R)	±0.01	<0.8	±0.14
Shear stress, Pa			(L) 0.003 (R)	?	<0.013	

[†] Uncertainties refer only to the model parameter estimation, and do not include the generally more significant factor of ~2 from model validation.

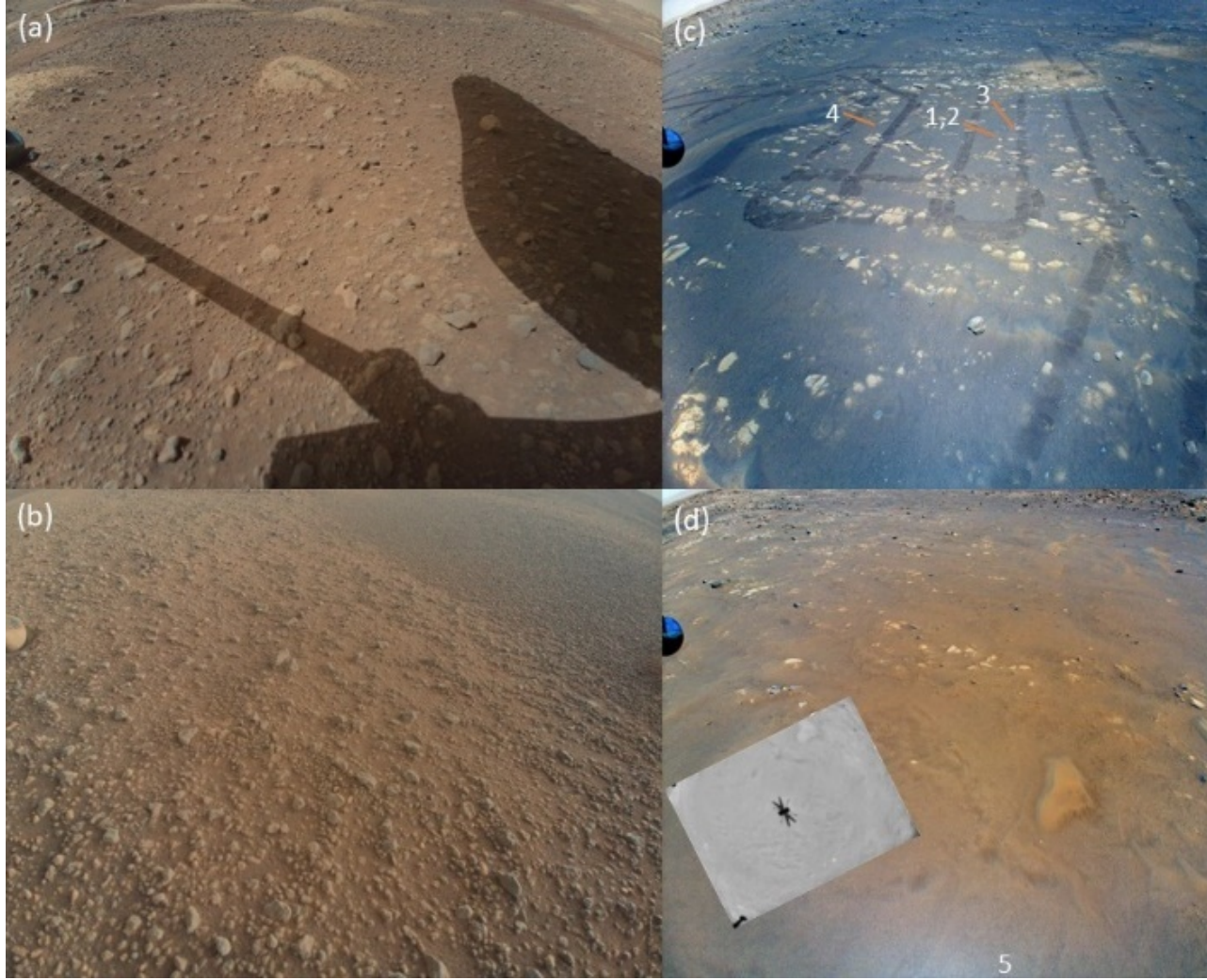


Figure 9. Landing suite characteristics in RTE images: (a) Sol-46 image prior to flight 1; (b) sol-214 image from flight-13 landing site; (c) sol 64 image from the return traverse, showing landing sites 1-4 and disturbed terrain; (d) sol-76 image with NAV inset showing flight-5 landing site.

4.3 Dust lifting during traverses

Dust lifting was seen on 4 of 5 traverses (among those that that exceeded 2 m length) at cruising altitude of 5 m AGL (5.1-5.7 m rotor height). One traverse at 5 m and both at 8 m had no observed lifting. For flight 3 outbound and inbound and flights 4 and 5 inbound, the model-predicted u^* was 0.26-0.29 m/s.

While the landing sites (Fig. 9) were selected based on smooth surfaces and other enabling characteristics, the traverses included more diversity of terrain.

We note that much terrain that was overflow did not produce dust lifting; heterogeneity of characteristics like dust availability and roughness resulted in heterogeneity of lifting outcomes. The flight-3 lifting was seen while the helicopter was over tracks that the rover had made (see bottom of Fig. 9c), while the other events were over terrain that was undisturbed or had been flown over from 5-m AGL.

Dust lifting on traverses requires mobilization and destruction of aggregates, as sand mobilization thresholds are not approached even if the model underpredicts by a factor of 2. The lifting occurs above the expected altitude for mobilization of aggregates (Fig. 7). A possible explanation is that some aggregates are not compact spheres as tested by Merrison et al. (2008), and filamentary aggregates may be more easily destroyed when they intrude into winds.

4.4 Implications for threshold velocity and dust lifting mechanisms

While there was only a small sample of observed dust lifting conditions, several observations are important. First, flights 5 and 13 were the only landings in undisturbed terrain. They had $u^* \sim 0.6\text{-}0.8$ m/s, or wind stress $\sim 5\text{-}13$ mPa. Second, flight 1 exhausted its dust source from 3.3-m height but found a new source at ~ 6 mPa during descent. Third, flights 1-3 all landed in disturbed terrain—not just the rover tracks visible in Fig. 9, but also the effects of taking off from the same site. They had $u^* \sim 0.4\text{-}0.5$ m/s, or surface shear stress $\sim 3\text{-}6$ mPa. Fourth, some areas had dust lifting at $u^* \sim 0.26\text{-}0.29$ m/s, or wind stress $\sim 1.4\text{-}1.7$ mPa.

These and earlier observations constrain dust lifting mechanisms in several ways. First, multiple mechanisms (or a significant variation in conditions) must have been relevant. Dust lifting occurred with 4x less wind stress during parts of traverses than at any landing site. Dust lifting stalled, then restarted during the first landing. Second, saltation likely played some role, at least in high background winds. Specifically, the flight 1 take-off appeared to initiate a saltation cluster that propagated downwind. Third, dust lifting was easier (had a lower threshold) in disturbed material (such as rover tracks or earlier flight paths) than undisturbed material. This is unsurprising, and consistent with observations of more sediment motion in disturbed vs. undisturbed material in a dust storm (Lemmon et al., 2022). Fourth, sand mobilization cannot explain all dust lifting. The predicted friction velocity for dust lifting on landing in undisturbed terrain was similar to predictions for sand mobilization at low pressure; and for undisturbed terrain the predicted friction velocity was within a factor of two of mobilization thresholds. Along traverses, dust lifting occurred at <0.3 m/s and cannot be explained with sand mobilization. It is likely that some places along the traverse had high dust content, and in those cases the dust formed large some mix of compact (Merrison et al., 2008) and filamentary (Sullivan et al., 2008) aggregates. This may reconcile observations of extensive lifted dust in dust devils and gusts with low abundance of sediment mobilizing events at the rover (Newman et al., 2022b). Future CFD simulations which can resolve the complex rotor-wake/ground interactions may allow more specific sediment

threshold mobilization constraints to be determined from these observations.

4.5 Dynamical behavior of lifted dust

When dust clouds formed, they expanded initially in all directions regardless of wind direction and speed. Within 2-3 s, the clouds elongated downwind with diffuse boundaries, and a curved and distinct boundary (front) was visible on the windward side. Pulses of lifted dust at takeoff and landing drifted away and became diffuse within seconds. Figure 10 shows example dust cloud motions. (See also Supplementary Movies.)

For the flight-4 dust cloud, there is a distinct recirculation pattern as dusty air was circulated up to rotor height and pushed back down. The flight-3 dust clouds also had the beginnings of such recirculation as tendrils of dust reached above the helicopter. In the flight-4 case, the recirculation organized the dust cloud around the helicopter: during the traverse, the cloud moved at the speed of the helicopter; once the helicopter had landed, the cloud drifted away at 1/3 the previous speed. During approach and landing, new dust was lifted, and the recirculating pattern narrowed as the rotors descended.

The Lorenz (2020) flux balance model, while it shows reasonable agreement with a set of dust loading measurements for several different helicopters, and with a set of dust density measurements for a hovering helicopter at different altitudes (Rodgers, 1968), predicts dust concentrations for *Ingenuity* about an order smaller than what we observe here, using the observed sedimentation velocity. While the basic physical framework of the model seems applicable, it seems the parameterization of dust flux with downwash velocity (derived from field measurements on Earth) requires adjustment for Mars application.

It is interesting to observe that the dust cloud masses we determine are of the order of 2 grams, or about 1/1000 of the mass of the *Ingenuity* vehicle itself. This may be compared with the dust cloud masses estimated for terrestrial helicopters in the ‘Sandblaster 2’ field tests using the data summarized in table 2 of Lorenz (2020). For the largest helicopter consider, the CH-53, the dust cloud (approximated as disk area times rotor height times dust density) approaches some 5 kg. All 5 cases for which data were available (UH-1, CH-46, HH-60, CH-53 and V-22) had dust clouds of 0.07-0.2 thousandths of the vehicle mass, indicating that while the dust clouds we have observed on Mars are small and thin, their generation is disproportionate.

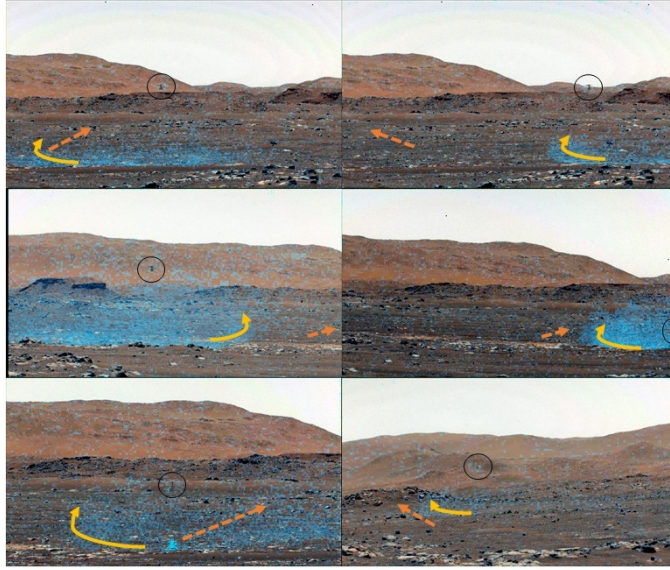


Figure 10: Dust clouds during traverse. Top: sol 64 outbound flight, return flight (from left); Middle: sol 69 traverse and landing; Bottom: Sol 58 hover and sol 76 traverse. Orange dashed arrows represent winds as seen from dust cloud advection. Yellow solid curves represent internal dust cloud motion. Circles show Ingenuity position.

5 Conclusions

We observed dust lifting during the take-off, traverse, and landing phases of six helicopter flights. During landings, the onset of dust lifting occurred when the helicopter was at altitudes of 1.4-3.6 m, with higher altitudes associated with more disturbed terrain. During 4 out of 5 traverse legs at 5-6 m altitude, dust lifting was observed away from the take-off or landing zone. Estimates of wind friction velocity at the time of onset of dust lifting were made using an existing sediment mobilization model. During landings at undisturbed locations, the onset of dust lifting was consistent with low-speed saltation models, suggesting that sand may have been mobilized as well. Dust removal from a track downwind of the helicopter on flight 1 also suggests the initiation of a saltation cluster. Disturbed areas produced dust with lower modeled wind speeds, although source exhaustion was observed during a hover, to be followed by renewed dust lifting as the winds increased during landing. During traverses, dust lifting was observed from heights at which saltation was unlikely, suggesting the likelihood of break-up of dust aggregates and entrainment of the resulting dust. Spatial heterogeneity was important: even within a single flight, dust lifting occurred in some areas but not others. Recirculating dust clouds were able to form around the helicopter on at least two flights from a 5-m cruising altitude, with an especially well-developed one on flight 4. While the geometric conditions (such as height) for which dust lifting occurred were well-constrained, a

more accurate prediction of surface shear stress will require CFD modeling.

Acknowledgments

The authors acknowledge and thank the Mars 2020 team. The research was carried out at the Jet Propulsion Laboratory, California Institute of Technology, under a contract with the National Aeronautics and Space Administration (80NM0018D0004). ML is supported by contract 15-712 from Arizona State University and 1607215 from Caltech-JPL. A. V.-R. is supported by the Spanish State Research Agency (AEI) Project No. MDM-2017-0737 Unidad de Excelencia “María de Maeztu”- Centro de Astrobiología (INTA-CSIC).

Open research

All Perseverance data used in this study are publicly available via the Planetary Data System (Bell and Maki, 2021; Maki, 2021; Rodriguez-Manfredi and de la Torre Juarez, 2021; Balaram, 2021).

References

- Ayoub, F., J.P. Avouac, C.E. Newman, M.I. Richardson, A. Lucas, S. Lepince, and N.T. Bridges (2014). Threshold for sand mobility on Mars calibrated from seasonal variations of sand flux. *Nature Communications* **5**, 5096. DOI: 10.1038/ncomms6096.
- Baker, M., C. Newman, C. Charalambous, M. Golombek, A. Spiga, D. Banfield, M. Lemmon, M. Banks, R. Lorenz, J. Garvin, J. Grant, K. Lewis, V. Ansan, N. Warner, C. Weitz, S. Wilson, S. Rodriguez (2021). Vortex-dominated aeolian activity at InSight’s landing site, Part 2: local meteorology, transport dynamics, and model analysis. *J. Geophys. Res.* **126**, E06514. DOI: 10.1029/2020JE006514.
- Balaram, J. (2021). Mars 2020 Helicopter Camera Suite Bundle. PDS Imaging Node. DOI: 10.17189/1522845.
- Balaram, J., M. Aung, and M.P. Golombek (2021) The Ingenuity helicopter on the Perseverance rover. *Space Sci. Rev.* **217**, 56. DOI: 10.1007/s11214-021-00815-w.
- Balaram, J., T. Canham, C. Duncan, M. Golombek, H.F. Grip, W. Johnson, J. Maki, A. Quon, R. Stern, and D. Zhu (2018). Mars Helicopter Technology Demonstrator. 2018 AIAA Atmospheric Flight Mechanics Conference, DOI: 10.2514/6.2018-0023.
- Bell, J. F., J.N. Maki (2021). Mars 2020 Mast Camera Zoom Bundle, from Arizona State University Mastcam-Z Instrument Team, calibrated products. PDS Imaging Node. DOI: 10.17189/q3ts-c749.
- Bell, J.F., III, J.N. Maki, G.L. Mehall, M.A. Ravine, M.A. Caplinger, Z.J. Bailey, S. Brylow, J.A. Schaffner, K.M. Kinch, M.B. Madsen, A. Winhold, A.G. Hayes, P. Corlies, C. Tate5 · M. Barrington, E. Cisneros, E. Jensen, K. Paris, K. Crawford, C. Rojas, L. Mehall, J. Joseph, J.B. Proton, N. Cluff, R.G. Deen, B.

Betts, E. Cloutis, A.J. Coates, A. Colaprete, K.S. Edgett, B.L. Ehlmann, S. Fagents, J.P. Grotzinger, C. Hardgrove, K.E. Herkenhoff, B. Horgan, R. Jaumann, J.R. Johnson, M. Lemmon, G. Paar, M. Caballo-Perucha, S. Gupta, C. Traxler, F. Preusker, M.S. Rice, M.S. Robinson, N. Schmitz, R. Sullivan, and M.J. Wolff (2021). The Mars 2020 Perseverance Rover Mast Camera Zoom (Mastcam-Z) Multispectral, Stereoscopic Imaging Investigation. *Space Science Reviews*, **217**, 24. DOI: 10.1007/s11214-020-00755-x.

Bila, T., G. Wurm, F. Chioma Onyeagusi, J. Teiser (2020). Lifting grains by the transient low pressure in a martian dust devil. *Icarus* **339**, 113569. DOI: 10.1016/j.icarus.2019.113569.

Charalambous, C., J.B. McClean, M. Baker, W.T. Pike, M. Golombek, M. Lemmon, V. Ansan, A. Spiga, R. Lorenz, M.E. Banks, N. Murdoch, S. Rodriguez, C.M. Weitz, J.A. Grant, N.H. Warner, J. Garvin, I.J. Daubar, E. Hauber, A.E. Stott, C.L. Johnson, A. Mittelholtz, T. Warren, S. Navarro, L.M. Sotomayor, J. Maki, A. Lucas, D. Banfield, C. Newman, D. Viúdez-Moreiras, J. Pla-Garcia, P. Lognonné, and W.B. Banerdt (2021). Vortex-dominated aeolian activity at InSight’s landing site, Part 1: Multi-instrument observations, analysis, and implications. *J. Geophys. Res.* **126**, e2020JE006757, E006757. DOI: 10.1029/2020JE006757.

Farrell, W.M., McLain, J.L., Marshall, J.R. and Wang, A., 2021. Will the Mars Helicopter Induce Local Martian Atmospheric Breakdown? *The Planetary Science Journal*, 2(2), p.46.

Greeley, R. (2002). Saltation impact as a means for raising dust on Mars. *Planetary and Space Science*, **50**, 151-155, [https://doi.org/10.1016/S0032-0633\(01\)00127-1](https://doi.org/10.1016/S0032-0633(01)00127-1)

Greeley R. and J D Iversen (1985). *Wind as a Geological Process on Earth, Mars, Venus, and Titan* (Cambridge Univ. Press, New York).

Greeley, R., P.L. Whelley, R.E. Arvidson, N.A. Cabrol, D.J. Foley, B.J. Franklin, P.J. Geissler, M.P. Golumbeck, R.O. Kuzmin, G.A. Landis, M.T. Lemmon, L.D.V. Neakrase, S.W. Squyres, S. D. Thompson, 2006. Active dust devils in Gusev Crater, Mars: Observations from the Mars Exploration Rover, Spirit. *J. Geophys. Res.* **111**, E12S09, doi: 10.1029/2006JE002743.

Grip, H.F., Conway, D., Lam, J., Williams, N., Golombek, M.P., Brockers, R., Mischna, M. and Cacan, M.R., 2022, March. Flying a Helicopter on Mars: How Ingenuity’s Flights were Planned, Executed, and Analyzed. In 2022 IEEE Aerospace Conference, Big Sky, Montana, 5-12 March 2022 doi:10.1109/AERO53065.2022.9843813

Guzewich, S.D., M. Lemmon, C.L. Smith, G. Martinez, A. Vicente-Retortillo, C.E. Newman, M. Baker, C. Campbell, B. Cooper, J. Gomez-Elvira, A.-M. Harri, D. Hassler, F.J. Martin-Torres, T. McConnochie, J.E. Moores, H. Kahanpaa, A. Khayat, M.I. Richardson, M.D. Smith, R. Sullivan, M. de la Torre Juarez, A.R. Vasavada, D. Viudez-Moreiras, C. Zeitlin, M.P. Zorzano Mier, 2019.

Mars Science Laboratory observations of the 2018/Mars year 34 global dust storm. *Geophys. Res. Lett.*, **46**, 71-79. DOI: 10.1029/2018GL080839.

Hayes, A.G., P. Corlies, C. Tate, M. Barrington, J.F. Bell, J.N. Maki, M. Caplinger, M. Ravine, K.M. Kinch, K. Herkenhoff, B. Horgan, J. Johnson, M. Lemmon, G. Paar, M.S. Rice, E. Jensen, T.M. Kubacki, E., R. Deen, B.L. Ehlmann, E. Lakdawalla, R. Sullivan, A. Winhold, A. Parkinson, Z. Bailey, J. van Beek, P. Caballo-Perucha, E. Cisneros, D. Dixon, C. , O.B. Jensen, J. Kuik, K. Lapo, A. Magee, M. Merusi, J. Mollerup, N. Scudder, C. Seeger, E. Stanish, M. Starr, M. Thompson, N. Turenne, and K. Winchell (2021) Pre-Flight Calibration of the Mars 2020 Rover Mastcam Zoom (Mastcam-Z) Multispectral, Stereoscopic Imager. *Space Science Reviews* **217**, 29. DOI: 10.1007/s11214-021-00795-x.

Herkenhoff, K.E., S. W. Squyres, R. Arvidson, D. S. Bass, J. F. Bell III, P. Bertelsen, N. A. Cabrol, L. Gaddis, A. G. Hayes, S. F. Hviid, J. R. Johnson, K. M. Kinch, M. B. Madsen, J. N. Maki, S. M. McLennan, H. Y. McSween, J. W. Rice Jr., M. Sims, P. H. Smith, L. A. Soderblom, N. Spanovich, R. Sullivan, and A. Wang (2004). Textures of the Soils and Rocks at Gusev Crater from Spirit's Microscopic Imager. *Science* **305**, 824-826. DOI: 10.1126/science.3050824.

Iversen, J.D., and B.R. White (1982). Saltation threshold on Earth, Mars and Venus. *Sedimentology* **29** (1), 111-119. <https://doi.org/10.1111/j.1365-3091.1982.tb01713.x>.

Kahre, M.A., Murphy, J.R., Newman, C.E., Wilson, R.J., Cantor, B.A., Lemmon, M.T., Wolff, M.J., 2017. The Mars dust cycle. In: Haberle, R., Clancy, R., Forget, F., Smith, M., Zurek, R. (Eds.), *The Atmosphere and Climate of Mars*. Cambridge University Press, pp. 295-337. DOI: 10.1017/9781139060172.010.

Kok, J.F., 2010. Difference in the Wind Speeds Required for Initiation versus Continuation of Sand Transport on Mars: Implications for Dunes and Dust Storms. *Phys. Rev. Lett.* **104**, 074502. DOI: 10.1103/PhysRevLett.104.074502.

Kraemer, A., J. Teiser, T. Steinpilz, M. Koester, and G Wurm (2019). Analog experiments on thermal creep gas flow through Martian soil. *Planet. and Space Sci.*, 166, 131-134. <https://doi.org/10.1016/j.pss.2018.09.004>.

Kruss, M., T. Salzmann, E. Parteli, F. Jungman, J. Teiser, L. Schöna, and G. Wurm (2021). Lifting of Tribocharged Grains by Martian Winds. *Planet Sci. J.* **2**:238. DOI: 10.3847/PSJ/ac38a4.

Lemmon, M.T., M.D. Smith, D. Viudez-Moreiras, M. de la Torre-Juarez, A. Vicente-Retortillo, A. Manguira, A. Sanchez-Lavega, R. Hueso, G. Martinez, B. Chide, R. Sullivan, D. Toledo, L. Tamppari, T. Bertrand, J.F. Bell III, C. Newman, M. Baker, D. Banfield, J.A. Rodriguez-Manfredi, J.N. Maki, V. Apestigue (2022). Dust, Sand, and Winds within an Active Martian Storm in Jezero Crater. *Geophys. Res. Lett.*, 49, e2022GL100126. DOI: 10.1029/2022GL100126.

Lorenz, R. D. 1993. Wake-Induced Dust Cloud Formation following Impact of

Planetary Landers' *Icarus* vol.101 pp.165-167

Lorenz, R.D., 2020. Triboelectric charging and brownout hazard evaluation for a planetary rotorcraft. In: AIAA AVIATION 2020 FORUM. <https://doi.org/10.2514/6.2020-2837>.

Lorenz, R. D. 2022. Planetary Exploration with Ingenuity and Dragonfly: Rotary-Wing Flight on Mars and Titan, American Institute of Aeronautics and Astronautics, ISBN 978-1-62410-636-1, 194pp.

Maki, J.N., D. Gruel, C. McKinney, M.A. Ravine, M. Morales, D. Lee, R. Willson, D. Copley-Woods, M. Valvo, T. Goodsall, J. McGuire, R.G. Sellar, J.A. Schaffner, M.A. Caplinger, J.M. Shamah, A.E. Johnson, H. Ansari, K. Singh, T. Litwin, R. Deen, A. Culver, N. Ruoff, D. Petrizzo, D. Kessler, C. Basset, T. Estlin, F. Alibay, A. Nelessen, and S. Algermissen¹ (2020). The Mars 2020 Engineering Cameras and Microphone on the Perseverance Rover: A Next-Generation Imaging System for Mars Exploration. *Space Sci. Rev.* **216**, 137. DOI: 10.1007/s11214-020-00765-9.

Maurice, S., B. Chide, N. Murdoch, R. D. Lorenz, D. Mimoun³, R. C. Wiens, A. Stott, X. Jacob, T. Bertrand, F. Montmessin, N. L. Lanza, C. Alvarez-Llamas, S. M. Angel, M. Aung, J. Balaram, O. Beyssac, A. Cousin, G. Delory¹², O. Forni, T. Fouchet, O. Gasnault, H. Grip, M. Hecht, J. Hoffman, J. Laserna, J. Lasue, J. Maki, J. McClean, P.-Y. Meslin¹, S. Le Mouélic, A. Munguira, C. E. Newman, J. A. Rodríguez Manfredi, J. Moros, A. Ollila, P. Pilleri, S. Schröder, M. de la Torre Juárez, T. Tzanetos, K. M. Stack, K. Farley, K. Williford, and the SuperCam team, 2022. In Situ Recordings of Mars Soundscape, *Nature*, **605**, pp. 653–658. <https://doi.org/10.1038/s41586-022-04679-0>

Merrison, J. P., Gunnlaugsson, H. P., Nørnberg, P., Jensen, A. E., and Rasmussen K. R. (2007). Determination of the wind induced detachment threshold for granular material on Mars using wind tunnel simulations. *Icarus*, 191, 568–580, doi:10.1016/j.icarus.2007.04.035

Moores, J., M.T. Lemmon, H. Kahanpää, S.C. Rafkin, R. Francis, J. Pla-Garcia, K. Bean, R. Haberle, C. Newman, M. Mischna, A. Vasavada, M. de la Torre Juárez, N. Rennó, J. Bell, F. Calef, B. Cantor, T.H. McConnochie, A.-M. Harri, M. Genzer, M. Wong, M.D. Smith, F. J. Martín-Torres, M.-P. Zorzano, O. Kемppinen, and E. McCullough (2015). Observational evidence of a shallow planetary boundary layer in northern Gale Crater, Mars as seen by the NavCam instrument onboard the Mars Science Laboratory Rover. *Icarus* **249**, 129-142. DOI: 10.1016/j.icarus.2014.09.020.

Musiolic, G., M. Kruss, T. Demirci, B. Schirinski, J. Teiser, F. Daerden, M.D. Smith, L. Neary, and G. Wurm (2018). Saltation under Martian gravity and its influence on the global dust distribution. *Icarus* **306**, 25-31. DOI: 10.1016/j.icarus.2018.01.007.

Neakrase, L.D.V., M.R. Balme, F. Esposito, T. Kelling, M. Klose, J.F. Kok, B. Marticorena, J. Merrison, M. Patel, and G. Wurm (2016). Particle Lifting

Processes in Dust Devils. *Space Sci. Rev.* **203**, 347-376. DOI 10.1007/s11214-016-0296-6.

Newman, C.E., M. de la Torre Juarez, J. Pla-Garcia, R.J. Wilsom, S.R. Lewis, L. Neary, M.A., Kahre, F. Forget, A. Spiga, M.I. Richardson, F. Daerden, T. Bertrand, D. Viudez-Moreairas, R. Sullivan, A. Sanchez-Lavega, B. Chide, and J.A. Rodriguez-Manfredi (2021). Multi-model Meteorological and Aeolian Predictions for Mars 2020 and the Jezero Crater Region. *Space Sci. Rev.* **217**:20. DOI: 10.1007/s11214-020-00788-2.

Newman, C.E., Bertrand, T., Fenton, L.K., Guzewich, S.D., Jackson, B., Lewis, S.R., Mischna, M.A., Montabone, L., Wellington, D.F. (2022a). Martian Dust, Ed.: Shroder, J.F., in Treatise on Geomorphology (2nd Ed.), Academic Press, 637-666, doi: 10.1016/B978-0-12-818234-5.00143-7, 2022a.

Newman, C.E., R. Hueso, M.T. Lemmon, A. Munguira, Á. Vicente-Retortillo, V. Apestigue, G. Martínez Martínez, D. Toledo Carrasco, R. Sullivan, K. Herkenhoff, M. de la Torre Juárez, M.I. Richardson, A. Stott, N. Murdoch, A. Sanchez-Lavega, M. Wolff, I. Arruego Rodriguez, E. Sebastián, S. Navarro, J. Gómez-Elvira, L. Tamppari, D. Viúdez-Moreiras, A.-M. Hari, M. Genzer, M. Hieta, R.D. Lorenz, P. Conrad, F. Gómez Gómez, T. McConnochie, D. Mimoun, C. Tate, T. Bertrand, J. Bell, J. Maki, J.A. Rodriguez Manfredi, R. Wiens, B. Chide, S. Maurice, M.-P. Zorzano, L. Mora, M. Baker, D. Banfield, J. Pla-Garcia, O. Beyssac, A. Brown, B. Clark, A. Lepinette, F. Montmessin, E. Fischer, P. Patel, T. del Río-Gaztelurrutia, T. Fouchet, R. Francis, and S. Guzewich, 2022b. The dynamic atmospheric and aeolian environment of Jezero crater, Mars. *Sci. Adv.* **8**, eabn3782, DOI: 10.1126/sciadv.abn3783. Rabinovitch, J., R. Lorenz, E. Slimko, and K.-S. C. Wang (2021). Scaling sediment mobilization beneath rotorcraft for Titan and Mars. *Aeolian Research* **49**, 100653. DOI: 10.1016/j.aeolia.2020.100653.

Reiss, D., L. Fenton, L. Neakrase, M. Zimmerman, T. Statella, P. Whelley, A.P. Rossi, and M. Balme (2016). Dust Devil Tracks. *Space Sci. Rev.* **203**, 143-181. DOI: 10.1007/s11214-016-0308-6.

Rodgers, S.J. "Evaluation of the dust cloud generated by helicopter rotor blade downwash". USAAVLABS Technical Report 67-81, U.S. Army Aviation Material Laboratories, 1968.

Rodriguez-Manfredi, J.A., and M. de la Torre Juarez (2021). Mars 2020 Perseverance Rover Mars Environmental Dynamics Analyzer (MEDA) Experiment Data Record (EDR) and Reduced Data Record (RDR) Data Products Archive Bundle. PDS Atmospheres Node. DOI: 10.17189/1522849.

Rodriguez-Manfredi, J.A., M. de la Torre Juárez, A. Alonso, V. Apéstigue, I. Arruego, T. Atienza, D. Banfield, J. Boland, M.A. Carrera, L. Castañer, J. Ceballos, H. Chen-Chen, A. Cobos, P.G. Conrad, E. Cordoba, T. del Río-Gaztelurrutia, A. de Vicente-Retortillo, M. Domínguez-Pumar, S. Espejo, A.G. Fairen, A. Fernández-Palma, R. Ferrándiz, F. Ferri, E. Fischer, A. García-

- Manchado, M. García-Villadangos, M. Genzer, S. Giménez, J. Gómez-Elvira, F. Gómez, S.D. Guzewich, A.-M. Harri, C.D. Hernández, M. Hietä, R. Hueso, I. Jaakonaho, J.J. Jiménez, V. Jiménez, A. Larman, R. Leiter, A. Lepinette, M.T. Lemmon, G. López, S.N. Madsen, T. Mäkinen, M. Marín, J. Martín-Soler, G. Martínez, A. Molina, L. Mora-Sotomayor, J.F. Moreno-Álvarez, S. Navarro, C.E. Newman, C. Ortega, M.C. Parrondo, V. Peinado, A. Peña, I. Pérez-Grande, S. Pérez-Hoyos, J. Pla-García, J. Polkko, M. Postigo, O. Prieto-Ballesteros, S.C.R. Rafkin, M. Ramos, M.I. Richardson, J. Romeral, C. Romero, K.D. Runyon, A. Saiz-Lopez, A. Sánchez-Lavega, I. Sard, J.T. Schofield, E. Sebastian, M.D. Smith, R.J. Sullivan, L.K. Tamppari, A.D. Thompson, D. Toledo, F. Torrero, J. Torres, R. Urquí, T. Velasco, D. Viúdez-Moreiras, S. Zurita, and the MEDA team (2021). The Mars Environmental Dynamics Analyzer, MEDA. A suite of environmental sensors for the Mars 2020 mission. *Space Sci. Rev.* **217**, 48. DOI: 0.1007/s11214-021-00816-9.
- Shao, Y., & Lu, H. (2000). A simple expression for wind erosion threshold friction velocity. *Journal of Geophysical Research*, 105(D17), 22437–22443. DOI: 10.1029/2000jd900304
- Sullivan, R., and J.F. Kok (2017). Aeolian saltation on Mars at low wind speeds. *J. Geophys. Res.*, **122**, 2111–2143, doi:10.1002/2017JE005275.
- Sullivan, R., R. Greeley, M. Kraft, G. Wilson, M. Golombek, K. Herkenhoff, J. Murphy, and P. Smith (2000). Results of the Imager for Mars Pathfinder windsock experiment. *J. Geophys. Res.*, **105**, E10, 24547-24562. doi: 10.1029/1999JE001234.
- Sullivan, R., R. Arvidson, J.F. Bell, R. Gellert, M. Golombek, R. Greeley, K. Herkenhoff, J. Johnson, S. Thompson, P. Whelley, and J. Wray (2008), Wind-driven particle mobility on Mars: Insights from Mars Exploration Rover observations at ‘El Dorado’ and surroundings at Gusev Crater. *J. Geophys. Res.*, **113**, E06S07, doi:10.1029/2008JE003101
- Swann, C., D.J. Sherman, and R.C. Ewing (2020). Experimentally Derived Thresholds for Windblown Sand on Mars. *Geophysical Research Letters*, 47, e2019GL084484. DOI: 10.1029/2019GL084484.
- Wolff, M., López-Valverde, M., Madeleine, J., Wilson, R., Smith, M., Fouchet, T., Delory, G., 2017. Radiative process: Techniques and applications. In: Haberle, R., Clancy, R., Forget, F., Smith, M., Zurek, R. (Eds.), *The Atmosphere and Climate of Mars*. Cambridge University Press, pp. 106–171. DOI: 10.1017/9781139060172.006.